Dalton Transactions

Accepted Manuscript

ROYAL SOCIETY OF CHEMISTRY

www.rsc.org/dalton

An amphidynamic inorganic-organic hybrid crystal of bromoplumbate with 1, 5-bis(1-methylimidazolium)pentane exhibiting multi-functionality of dielectric anomaly and temperature-dependent dual band emissions

Yuan-Bo Tong,[a,b] Li-Te Ren,[b] Hai-Bao Duan,*[c] Jian-Lan Liu,[a] Xiao-Ming Ren*[a,b,c,d]

[a] State Key Laboratory of Materials-Oriented Chemical Engineering and College of Science, Nanjing Tech University, Nanjing 210009, P. R. China

[b] College of Materials Science and Engineering, Nanjing Tech University, Nanjing 210009, P.R. China

[c] School of Environmental Science, Nanjing Xiao Zhuang University, Nanjing 211171, P. R. China.

[d] State Key Lab & Coordination Chemistry Institute, Nanjing University, Nanjing 210093, P. R. China

Tel.: +86 25 58139476

Fax: +86 25 58139481

Email: xmren@njtech.edu.cn (RXM)

Abstract

An organic-inorganic hybrid crystals, [1, 5-bis(1-methylimidazolium)pentane]-$[PbBr_3]_2$ (**1**), were achieved through mutual diffusion of bi-imidazolium based ionic liquid and $PbBr_2$ solution of DMF in a glass tube. The hybrid solid crystallizes in orthorhombic space group *Fdd2* at room temperature; and is comprised of one-dimensional $[PbBr_3]_\infty$ chains where the neighboring $PbBr_6$ coordination octahedra are linked together via face-sharing mode and the inorganic chains are surrounded by organic cations. The hybrid solid exhibits dielectric anomaly around 443 K and dielectric relaxation above 400 K, the dielectric response mechanism was investigated by variable-temperature X-ray single crystal and powder diffraction as well as DSC techniques. Fascinatingly, this hybrid solid shows dual band emissions, moreover, the fluorescence nature of two emission bands exhibits distinct response to temperature, leading to displaying temperature-dependent fluorescence color, this feature has promising application in the emission temperature-sensing field.

Keywords: Haloplumbate hybrid; dielectric anomaly; dielectric relaxation; dual band luminescence; temperature-dependent emission

Introduction

Multifunctional materials that exhibit different physical properties in a single phase have potential for use in multifunctional devices.[1-5] A typical multifunctional material is ferromagnetic semiconductor that combines the capabilities of semiconductor quantum structures and ferromagnetic multilayers for simultaneous electrical, magnetic or optical responses.[6,7] In addition, the magnetically tunable band gap[8] and control of magnetism by means of electric fields[9,10] are simultaneously achievable in a ferromagnetic semiconductor owing to the existence of large sp-d exchange interaction between the band electrons and the magnetic transition metal ions. Another representative example is multiferroic material that the coexistence of magnetism and ferroelectricity is even more desirable for constructing multifunctional devices. [11,12]

Besides the above-mentioned multifunctional materials that the different functionalities are mutually coupling, another category of multifunctional material shows only the coexistence of multiple properties, such a material also has promising application in the devices with multiple channels responding to external stimuli.[13-16] For example, Sun and coworkers[13] reported a series of ionic iridium(III) complexes simultaneously exhibiting mechanochromic, vapochromic and electrochromic phosphorescence, and the corresponding data-recording device demonstrated that the multiple data encryption and decryption is achievable via fluorescence lifetime imaging and time-gated luminescence imaging techniques, respectively.

Up to date, in spite of challenges still remain in the synthesis of material with desirable multifunctional properties, it is an efficient strategy for design and preparation of such a material to combine molecular architectures with different types of functionality in a single phase, this is so-called 'multifunctional integrating strategy'. For instance, Tao et al.,[17] recently achieved a fluorescent spin-crossover (SCO) hybrid by grafting fluorophores (1-pyrenecarboxaldehyde and Rhodamine B) on one-dimensional SCO Fe^{II} structures, such hybrid materials display expected one-step SCO behavior and fluorescent properties, particularly showing a coupling between the transition temperature of SCO and the temperature where the fluorescent intensity reverses.

In the context of multifunctional material, we target at the dielectric and fluorescent ones based on the haloplumbate hybrids, because they have fertile

structures from one- to three-dimension,[18-21] tunable band gaps[22,23] and novel fluorescence nature.[24] In addition, it is noted that a haloplumbate-based amphidynamic crystal with anisotropic molecular order and controllable dynamics[25,26] is achievable if the building blocks with volume-conserving motion (dynamic disorder) are introduced into the haloplumbate hybrid lattice, since the disorder-to-order structural transformation frequently occurs in an amphidynamic crystal, this is widely believed to be coupled to dielectric anomales,[27-33] such a haloplumbate-based amphidynamic crystal probably displays novel dielectric and fluorescent properties simultaneously.

The imidazolium-based organic cations have been broadly used for making an ionic liquid since the imidazole ring shows low energy barrier of rotational and orientational motion in lattice, which is an ideal building block for constructing an amphidynamic crystal. In this paper, we present a hybrid crystal [1,5-bis(1-methyl-imidazolium)pentane][$PbBr_3$]$_2$ designed by the 'multifunctional integrating strategy', this hybrid solid really shows bi-functionality of dielectric anomaly and temperature-dependent dual band emissions.

Experimental section

Chemicals and materials

All reagents and chemicals were purchased from commercial sources and used without further purification. 1,5-bis(1-methylimidazolium)pentane bisbromide, was synthesized according to the similar procedure described in the literature.[34]

Preparation of 1

[1, 5-bis(1-methylimidazolium)pentane][$PbBr_3$]$_2$ (1) This hybrid crystals were achieved using the process below: $PbBr_2$ (0.01mol) mixed KBr (0.012 mol) in DMF (25 mL) and then heated to 60 °C for 3 hours until all solid dissolved and the mixture is labeled as solution-A; 1-methylimidazole (0.01 mol) and 1,5-dibromopentane (0.01 mol) were added in acetone (10 mL), then heated to 80 °C for 12 hours until turned yellow viscous fluid, which is washed with ethyl acetate, and then mixed with 25 mL DMF, this mixture is labeled as solution-B. Colorless needle-like crystals were obtained by diffusion of solution-A and solution-B in a glass tube four weeks later,

and the crystals were collected by suction and washed with a little amount of DMF and methanol in turn. Yield ~69%. Anal. Calc. for $C_{13}H_{22}Br_6N_4Pb_2$: C, 13.83; H, 1.95; N, 4.96%. Found: C, 13.88; H, 2.03; N, 4.90%.

The purity of **1** was examined with elemental analyses of C, H and N and powder X-ray diffraction (Fig. S1).

Physical measurements

Elemental analyses (C, H and N) were performed with an Elementar Vario EL III analyzer. Thermogravimetric (TG) analysis was performed on a SDT Q600 V20.9 Build 20, in the temperature ranges of 303–873 K under nitrogen atmosphere, and the heating rate is 5 K min^{-1}. Differential Scanning Calorimetry (DSC) measurement was carried out on a NETZSCH DSC 204F1 Phoenix for powder sample between 273 K and 473 K, with a temperature scanning rate of 5 K min^{-1}. IR spectra at room temperature were recorded on a Bruker VERTEX80V Fourier transform infrared spectrometer (KBr disc). Powder X-ray diffraction (PXRD) data were collected on a Bruker D8 Advance powder diffractometer operating at 40 kV and 40 mA using Cu Kα radiation with λ = 1.5418 Å. Samples were scanned 2θ from 5 to 50°. The measurements of temperature, frequency dependent dielectric permittivity were carried out using a concept 80 system (Novocontrol, Germany) in the temperature ranges of 123-473 K, the sample was prepared in the form of a disk with a 10 mm diameter and ca.0.86 mm thickness, and the disk was sandwiched between two parallel copper electrodes; the ac electrical field frequencies span from 1 to 10^7 Hz. Fluorescence spectra were recorded on a Fluorolog Tau-3 Fluorometer for the powdered crystalline sample at selected temperature. UV-visible absorption spectra were recorded on a PerkinElmer LAMBDA 950 UV/Vis/NIR spectrophotometer for solid sample at ambient temperature.

X-ray single crystallography

Single-crystal X-ray diffraction data for **1** were collected at 298, 373 and 413 K using graphite monochromated Mo Ka (λ= 0.71073 A) radiation on a CCD area

detector (Bruker-SMART). Data reduction and absorption corrections were performed with the SAINT and SADABS software packages,[35] respectively. Structures were solved by a direct method using the SHELXL-97 software package.[36] The non-hydrogen atoms were anisotropically refined using a full-matrix least-squares method on F^2. All hydrogen atoms were placed at the calculated positions and refined as riding on the parent atoms. The details of data collection, structure refinement and crystallography are summarized in Table 1. The C(2) atoms was refined using disorder model with two sites at 298 K and the site occupation factors were refined.

Table 1: Crystallographic data and refinement parameter of **1**

Temperature (K)	298(2)	373(2)	413(2)
Wavelength (Å)	0.71073	0.71073	0.71073
Empirical formula	$C_{13}H_{22}Br_6N_4Pb_2$	$C_{13}H_{22}Br_6N_4Pb_2$	$C_{13}H_{22}Br_6N_4Pb_2$
Formula weight	1128.14	1128.14	1128.14
CCDC no.	1405651	1411960	1411965
Crystal system	Orthorhombic	Orthorhombic	Orthorhombic
Space group	*Fdd2*	*Fdd2*	*Fdd2*
a (Å)	29.498(4)	29.787(5)	29.942(5)
b (Å)	22.319(3)	22.327(4)	22.309(4)
c (Å)	7.7732(9)	7.8007(12)	7.8155(11)
α (°)	90.00	90.00	90.00
β (°)	90.00	90.00	90.00
γ (°)	90.00	90.00	90.00
V (Å^3)/Z	5117.6(11)/8	5187.9(16)/8	5220.6(14)/8
ρ (g·cm^{-1})	2.929	2.889	2.871
F(000)	3968	4016	4016
Flack parameter	0.07(2)	0.02(4)	0.04(4)
Abs. coeff. (mm^{-1})	22.516	22.212	22.073
θ Ranges (data collection; °)	2.289 - 25.494	2.28-25.49	2.28-25.50
Index ranges	$-35 \le h \le 35$	$-36 \le h \le 33$	$-36 \le h \le 33$
	$-26 \le k \le 26$	$-24 \le k \le 26$	$-24 \le k \le 26$
	$-9 \le l \le 8$	$-9 \le l \le 9$	$-9 \le l \le 9$
R_{int}	0.00599	0.1070	0.1061
Independent reflections/restraints/parameters	2275/1/126	2375/1/116	2390/1/116
Refinement method	Full-matrix least-squares method on F^2		
Goodness of fit on F^2	1.007	1.026	1.022
R_1, wR_2[a] [$I>2\sigma$(I)]	0.0346, 0.0728	0.0572,0.1355	0.0599,0.1436

R_1, wR_2[a] [all data]	0.0568, 0.0778	0.1018,0.1579	0.1028,0.1681
Residual ($e \cdot nm^{-3}$)	1.000/-1.750	1.732/-1.940	1.733/-1.880

[a] $R_1 = \sum||F_o| - |F_c||/|F_o|$, $wR_2 = [\sum w(\sum F_o^2 - F_c^2)^2/\sum w(F_o^2)^2]^{1/2}$

Result and discussion

Crystal structure

Hybrid **1** crystallizes in non-centrosymmetric orthorhombic space group *Fdd2* at 298 K in low temperature phase. The asymmetric unit, as shown in Fig. 1a, consists of one Pb^{2+} ion and three different Br^- anions together with one half of 1,5-bis(1-methylimidazolium)pentane dication. Pb^{2+} ion is located at an inversion center and coordinated with six Br^- to form the slightly distorted $PbBr_6$ octahedron. The Pb-Br lengths range from 2.932(2) to 3.194(3) Å and the Br-Pb-Br angles fall within the ranges of 81.47(8)-179.66(5)° at 298 K, these geometry parameters within the coordination octahedron are comparable to other bromoplumbates.[37] Three different Br^- ions adopt in the μ_2-bridged model to connect two neighboring Pb^{2+} ions. The adjacent $PbBr_6$ coordination octahedra are connected together via face-sharing mode to form uniform $[PbBr_3]_\infty$ chain along the *c*-axis direction (Fig. 1b).

The dication is composed of a hydrocarbon chains and two 1-methylimidazolium head cores and possesses the symmetry of C_2 point group. The 2-fold rotation axis passing through the C(1) atom is parallel to the crystallographic *c*-axis. The hydrocarbon chain adopts in the completely trans-planar conformation, and two 1-methyl-imidazolyl rings show different orientations and the mean-molecule planes of two imidazolyl rings make a dihedral angle of 28.5º. The neighboring dications are aligned into the hexagon-shaped 1D channels along the *c*-axis direction, and the inorganic $[PbBr_3]_\infty$ chains reside in the channels (Fig.1c). The charge-assisted H-bonding interactions appear between the CH_2 groups in the dications and the Br^- ions in the inorganic chains with $d_{H(6)\cdots Br(3)}$ = 2.775 Å and $d_{H(3A)\cdots Br(1)\#2}$ = 3.033 Å (ref. Fig. S4 and symmetric codes: #1 = -x, 1.5+y, 1+z and #2 = 1-x, 2-y, z).

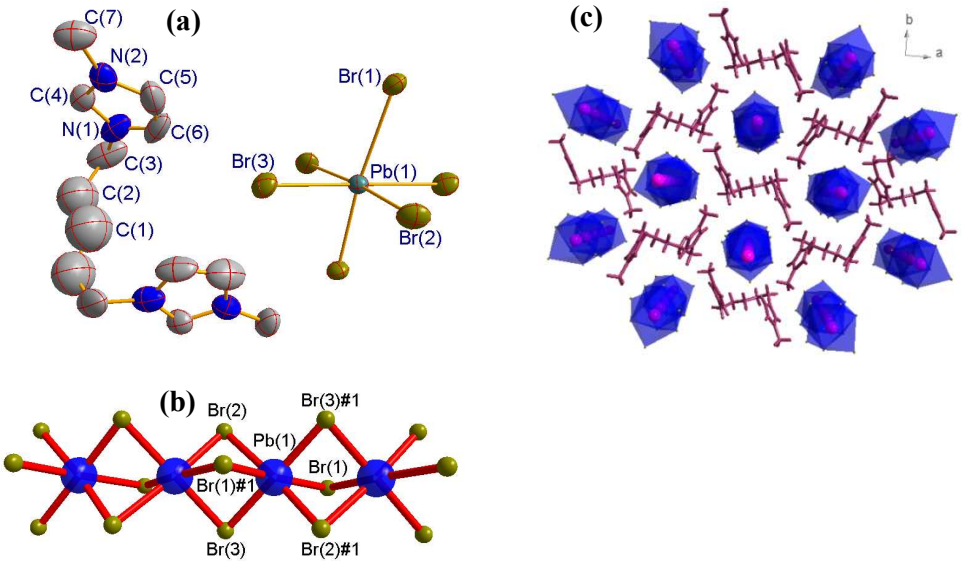

Fig.1: (a) Molecular structure of **1** at 298 K with non-hydrogen atom labeling and thermal ellipsoids drawn at the 50% probability level. (b) Face-sharing octahedral chain of $[PbBr_3]_\infty$and (c) Packing diagram viewed along the *c*-axis direction (the symmetric codes: # 1= 0.75+x, 1.25-y, -0.25+z).

Phase transition

The plots of real (ε') and imaginary (ε") parts of dielectric permittivity vs. temperature are shown in Fig. 2a and Fig. 2b for **1**, respectively. The plots of ε'-T display the characters (1) the dielectric permittivity is temperature-independence with $\varepsilon' \approx 12$ when the temperature is below 323 K, indicating that the thermally activated dipole motion is suppressed in the low temperature; then increases quickly and depends strongly on the ac frequency when the temperature is above 375 K. This observation demonstrates the existence of dielectric relaxation at elevated temperature. (2) A remarkable dielectric anomaly appears at ca. 443 K, and the peak maximum slightly shifts towards high temperature as frequency increases.

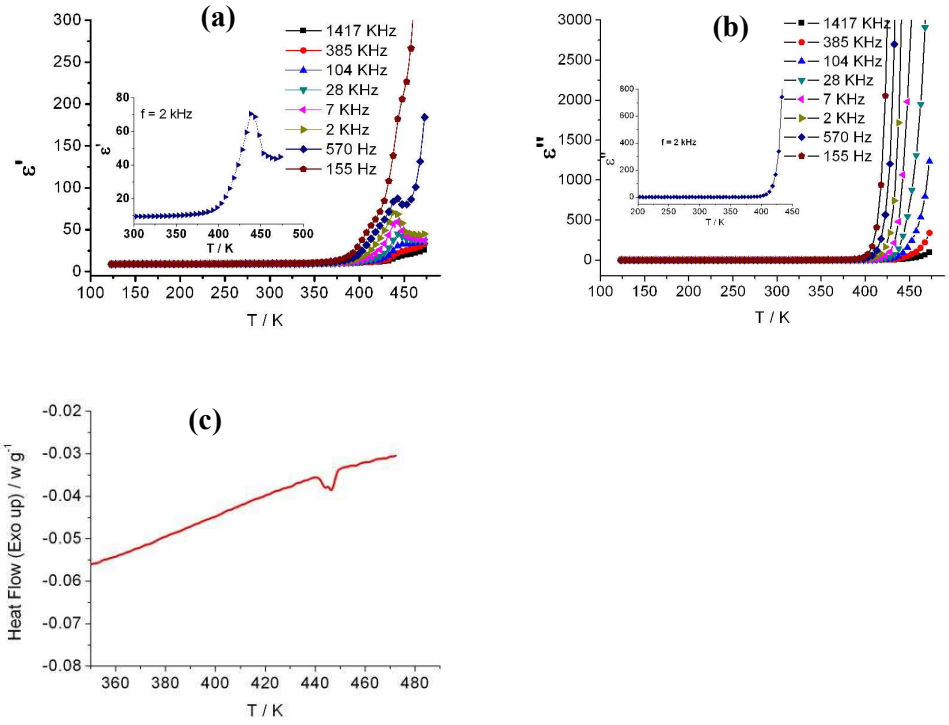

Fig. 2: (a, b) Plots of real (ε') and imaginary (ε") parts of dielectric permittivity versus temperature in 123-473 K at selected frequencies and plot in the inset at f = 2 kHz (c) DSC curve in a heating run in 350-473 K for **1**.

The DSC plot is displayed in Fig.2c for **1**, be indicative of two sequential endothermic events in the heating run. Two quite close thermal anomaly peaks locate at ca. 440 K and 446 K, respectively, and these are close to the peak temperature of dielectric anomaly. This observation further conform two sequential phase transitions undergoing around 443 K. The whole values of ΔH and ΔS were estimated to be 0.284 $kJ \cdot mol^{-1}$ and 0.634 $J \cdot K^{-1} \cdot mol^{-1}$ for two sequential phase transitions, respectively. The small values of ΔH and ΔS indicate that the phase transitions at ca. 443 K are probably related to the strong thermal vibrations of crystal lattice. It is certainly that the crystal structure in high-temperature phase could address clearly this issue; unfortunately, we failed to obtain details of the crystal structure in the high temperature phase due to the poor quality of the single crystal X-ray diffraction data above the phase transition. And then we determined the single crystal structure of **1** at 373 and 413 K in low-temperature phase, respectively, to inspect the atomic

displacements at different temperatures, and performed variable temperature powder X-ray diffraction data collection across the phase transition as well. From Table 1, it is found that the cell volume *V* of **1** expends by 1.37% from 298 to 373 K versus 2.01% from 298 to 441 K, indicating that the change of *V* is not so significant. As shown in Table 2, the atomic displacements related to the molecule motion increases quickly for all atoms with rising temperature, especially, for the atoms in the cation moiety, indicating that the dynamic motions of cations become more vigorous, as elevated temperature, regarding the $[PbBr_3]_\infty$ anion chain.

The PXRD profiles are shown in Fig. 3a at the selected temperatures for **1**, demonstrating that the position of diffraction peak are almost not changed within the range of 2θ = 5-50° in low- and high-temperature phases, however, the diffraction intensities decrease dramatically above the temperature of phase transition within the range of 2θ = 25-45° (Fig. 3b), this situation is quite similar to observation in the liquid crystals.[38, 39] These results further confirmed the existence of small structural difference between high- and low-temperature phases.

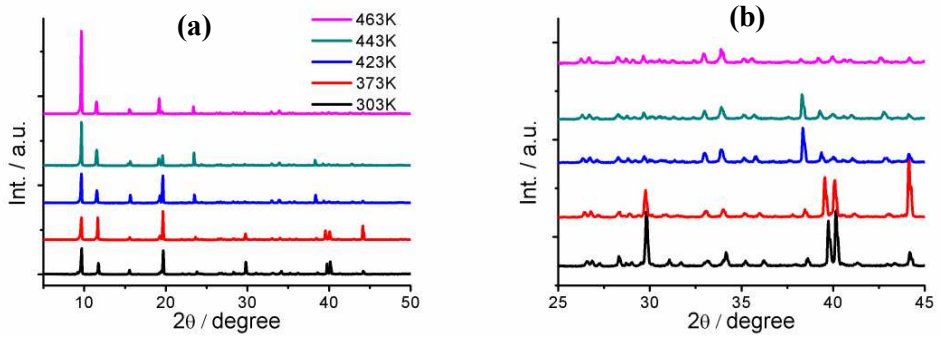

Fig. 3: Variable-temperature PXRD profiles of **1** in the ranges of (a) 2θ = 5-50° (b) 2θ = 22-45°.

Dielectric relaxation

The frequency dependences of ε' and dielectric loss (tanδ) are plotted in Fig.4 for **1**. The ε' value drops rapidly in the region of 1-10^5 Hz (ref. Fig.4a and 4b), demonstrating that the dynamical dipole motion cannot follow the quickly switching of the applied electric field at higher frequencies (f > 10^5 Hz). The curves of ε' and

tanδ against frequency (f) show clear difference between low- and high-temperature phases; the distinction appears in the f > 10^3 Hz regime in the ε'-f plots, and one rounded maximum emerges in the tanδ-f plots in low-temperature phase while two peaks are visible in high-temperature phase. The rounded maximum is strongly dependent on the ac frequency in both low- and high-temperature phases, whereas the position of sharp peak is weakly dependent on the ac frequency in high-temperature phase in the tanδ-f plots. The frequency-dependent dielectric permittivity and rounded maximum of dielectric loss (ref. Fig.4c and 4d) indicate the existence of dielectric relaxation in **1**. The Arrhenius equation $\tau = \tau_0 \exp(E_a/k_BT)$ was used for analysis of relaxation behavior, and τ_0 is the inverse of the frequency factor, represents macroscopic relaxation time, $\tau = 1/f_{max}$ and f_{max} is the maximums of tanδ vs. frequency plot at selected temperature, E_a denotes the activation energy of relaxation process, and other symbols in Arrhenius equation have normal meanings. The best fit for the lnτ vs. 1000/T plot gave the parameters: $\tau_0 = 2.53\times10^{-18}$ s and $E_a = 1.383$ eV for the dielectric relaxation (ref. Fig.5), these parameters are comparable to those in organic-inorganic hybrid $[C_2H_{10}N_2][SnCl(NCS)_2]_2$.[40]

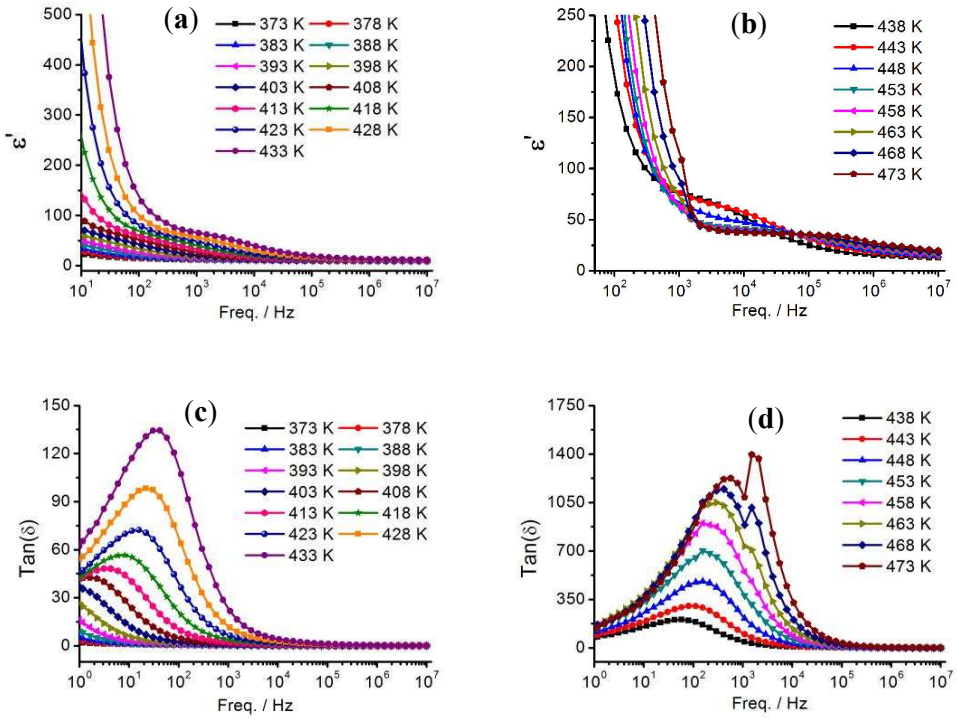

Fig. 4: (a, b) Plots of dielectric permittivity vs. frequency (c, d) dielectric loss (tanδ) vs. frequency at selected temperatures for **1**.

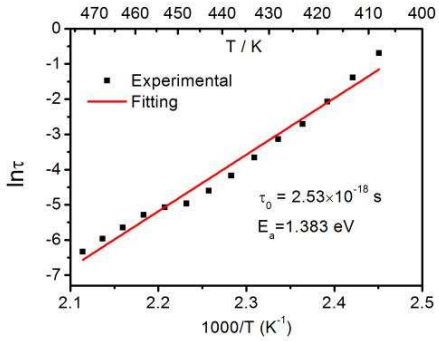

Fig. 5: Plots of lnτ vs. 1000/T of **1** for the relaxation in low frequency region.

The response frequency falls within the regime >10^{12} Hz for the dielectric relaxation originated from the electronic transitions or the bond vibrations within a molecule or an ion-pair, and in the region <10^{10} Hz for the dielectric relaxation arose from the molecular dipole motion or ionic migration.[41] The dielectric relaxation undergoing below the frequency of 10^5 Hz is probably related to the dynamic dipole motion of cations and relative displacement of cations regarding rigid $[PbBr_3]_\infty$ anionic chains. To better understand the dielectric relaxation process, we further analyze the ionic conducting behavior of **1**. The impedance plots are shown in Fig.6a and 6b for **1** at selected temperatures. A clear semicircle appears above 378 K in the Z''-Z' plot, and its radius decreases with increasing temperature, which indicates that the decrease of the bulk resistance with rising temperature owing to the relative motion of cations thermally activated at elevated temperature. The impedance plots were fitted using equivalent circuit, where each impedance semicircle can be represent by a resistor, R, and capacitor, C, in parallel. For instance, the Z''-Z' plot at 473K was fitted using above-mentioned equivalent circuit to give σ_{DC} = 7.014×10^{-5} S cm^{-1}. The temperature dependent conductivity σ_{dc} is plotted in the form of lnσ_{dc}T vs. 1000/T, as shown in Fig.6d, which shows linear relationship in the temperature range of 438-473 K, and the activation energy (E_a) was estimated to be 1.79 eV, this value is comparable with that obtained from dielectric relaxation analysis. On the basis of both dielectric and impedance spectra analysis, it is concluded that the dielectric relaxation

occurring below 10^5 Hz is attributed to the dipole oriental motion of imidazole rings in cations and ionic conduction of cations.

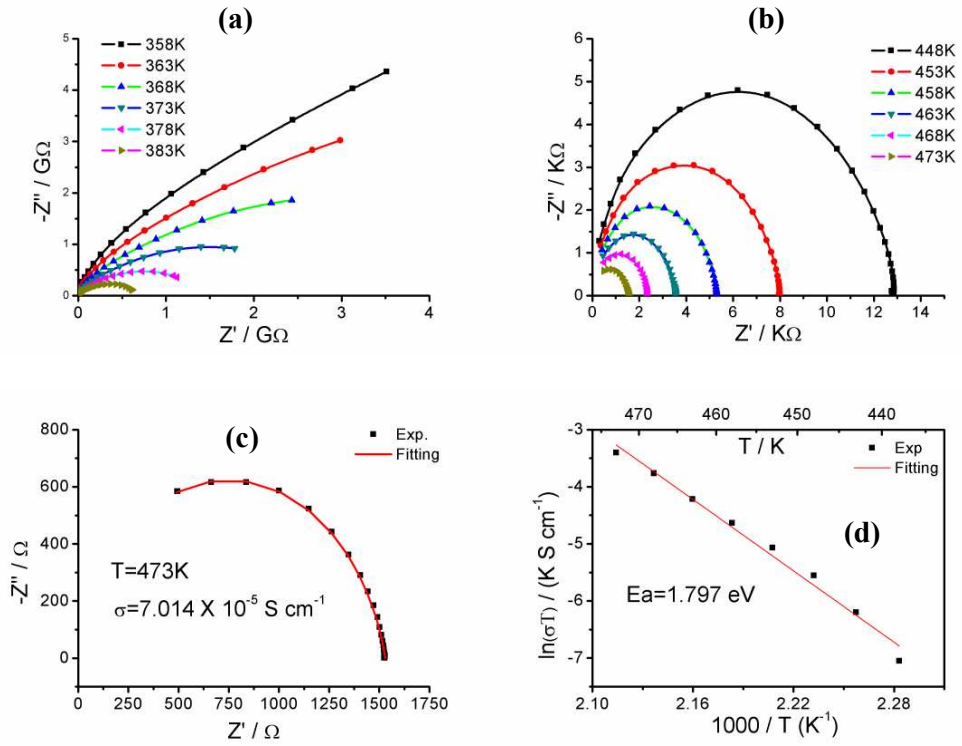

Fig. 6: (a, b) Typical Nyquist plots at selected temperatures (c) fitting for Nyquist plot at 473 K and (d) Arrhenius plots for **1**.

UV-vis, luminescent spectra and electronic band structure

Fig. 7a shows the optical absorption spectra of **1** in the solid state at room temperature, indicating the existence of intense absorption below 400 nm. One sharp peak locates at ca. 210 nm and a broad and asymmetric peak is centered at ca. 320 nm, these absorption bands are assigned to the electron transition of π*←π within the imidazole rings and from valence band to conducting band within the one-dimensional inorganic $PbBr_3^-$ chains.[42] The band assignment is supported by electronic band structure analysis (ref. Fig. S6). The optical band gap is estimated to be 3.44 eV for the one-dimensional inorganic $PbBr_3^-$ chain and comparable to the calculated value (3.57 eV), demonstrating the semiconductor character.

The excitation and emission spectra at selected temperatures are displayed in Fig.

7b and Fig. 7c for the powder sample of **1**. The excitation spectra exhibit two intense bands in the range of 280-360 nm at low temperature, and two peaks centered at 300 nm and ca. 330 nm (Fig.7b). The peak position of the band centered at 300 nm is independent on temperature, while the peak position of low energy band centered at ca. 330 nm shifts towards short wavelength side upon cooling, and the intensity of both excitation bands increases significantly with decreasing temperature (ref. Fig. 7b). As shown in Fig. S7, hybrid **1** shows weak fluorescence at 300 K upon excitation of λ_{ex} = 323 nm, a complicated broad emission band extends from 400 nm to 800 nm and a maximum locates at ca. 607 nm together with three shoulders at ca. 410, 570 and 680 nm. As the temperature decreases, the obviously dual emission bands were observed and centered at 450 nm and 680 nm (ref. Fig. S8). The whole fluorescence intensity is quite sensitive to the temperature, for example, the relative intensity at 10 K is as ca. 1000 times as that at 300 K. The influence of temperature on the fluorescence intensity is seen more clearly from Fig.8a-8c for two emission bands, where I_1 (S_1) and I_2 (S_1) represent the fluorescence intensity (peak area) of the shorter wavelength and longer wavelength emission bands, respectively. It was found that (1) the fluorescence intensity and the peak area show similar tread with temperature changing for two emission bands; (2) the fluorescence intensity and the peak area exhibit monotonous increase for the shorter wavelength emission band whereas complicated change for the longer wavelength emission band upon cooling.

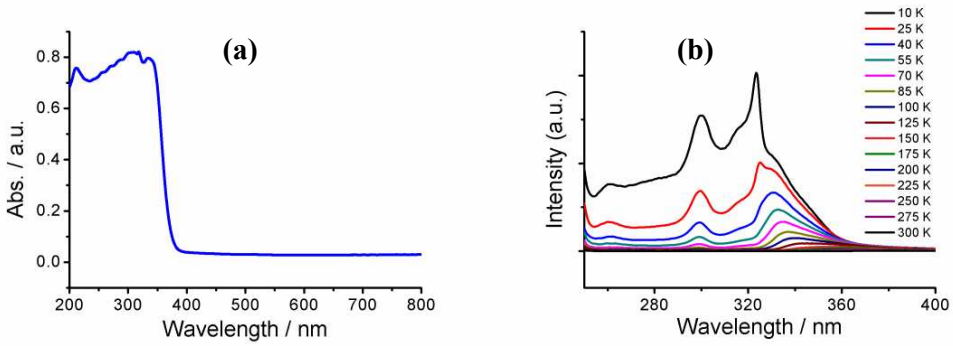

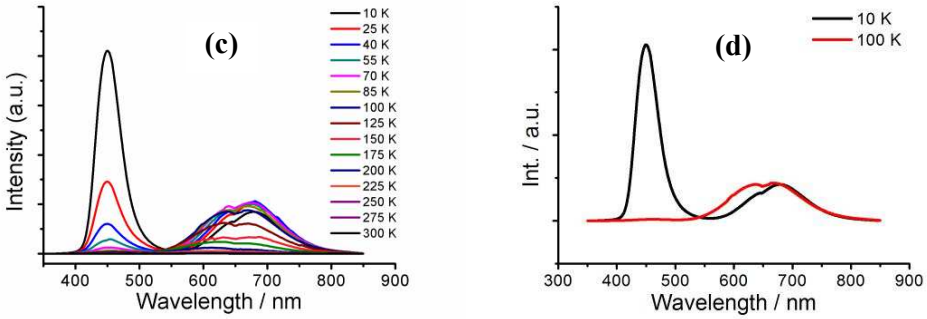

Fig. 7: (a) UV-Vis absorption spectrum (b) excitation and (c, d) emission spectra of **1** at selected temperatures.

It is well understood for the enhancement of emission in low temperature owing to the decay process of the lowest excited state nonradiative internal conversion to the ground state easy undergoing in high temperature regarding low temperature. It is noted that the shorter wavelength emission band center is independent on the temperature while its intensity is quite sensitive to temperature, as well as the band maximum slightly moves to the high energy side and the fluorescence intensity increases slowly for the longer wavelength emission band upon cooling. Generally, the emission spectra of molecule and semiconductor show distinct characters in band width and response to temperature. The band emitting from molecule shows narrow half width of peak and temperature-independent band center with respect to the broad half width of peak and temperature-dependent band center observed in a semiconductor. The half width of peak of emission band is related to the vibration level distribution of ground state in molecule or the width of valence band in semiconductor (from the bottom to the top of valence band). By contrast with the width of valence band in a semiconductor, the vibration level distribution of ground state in the molecule is quite narrow. The temperature change affect the vibration population in ground electronic state for a molecule or the valence band electron population in a semiconductor, thus, the influence of temperature change on the transition energy is more significant for the emission of semiconductor than that of the molecule. On the basis of the analysis above, the shorter and longer wavelength emission bands in **1** are assigned to $\pi \leftarrow \pi^*$ electron transition within the imidazole

rings and the electron transition from conducting band to valence band within the one-dimensional $PbBr_3^-$ chains, respectively.

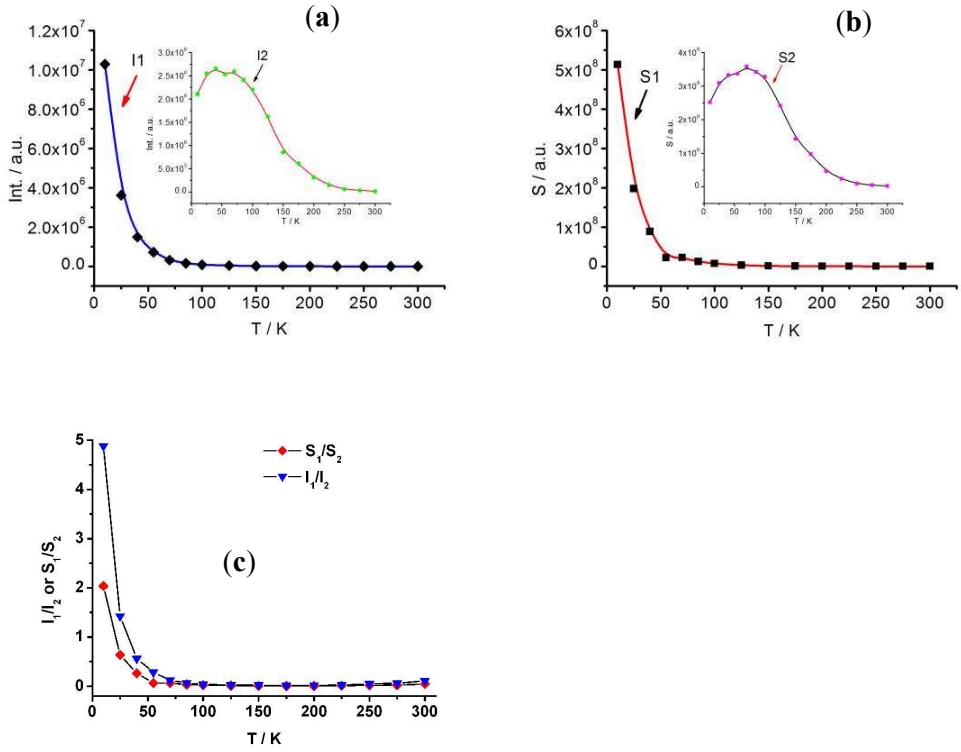

Fig.8: (a) Peak intensity and (b) Peak area of PL spectrum at selected temperature (c) Peak intensity and area ratio at selected temperatures.

The intensity ratio between two emission bands is quite sensitive to temperature for **1**, as a result, the emission color gradually evolves from blue to orange from 10 to 300 K. The corresponding CIE coordinates of **1** exhibit an easy intuitive change (Fig.9 and Table S2), a typical blue light emission occurs in the temperature ranges of 10-25 K, and with the CIE coordinate of (0.19, 0.08) at 10 K and (0.28, 0.14) at 25 K, respectively. When the temperature increased to 40 K, the emission color is red, the CIE coordinate is (0.39, 0.21). From 40 to 100 K, the emission color gamut shift slowly from red to orange. As the temperature is close to 125 K, hybrid **1** emits orange light, its' CIE coordinate locates at (0.58, 0.39). The emission color has a mild change when temperature is above 125 K and it mainly keep in the region of orange until the temperature up to 300 K. The luminescent materials, which emission natures

are sensitive to environment, have wide and potential applications as chemical sensors. A vapoluminescence material, which is the matter referring to changes in photoluminescence properties in the course of vapor exposure, such a material can be used for detection of other analytes (e.g., oxygen, humidity in air, ions in solution, acids or bases,[14] some volatile organic compounds).[43] Most recently, Tang and coworkers[44] reported an ytterbium complex, [$Yb(tta)_3$DFQZ] where Htta = thenoyltrifluoroacetone and DFQZ = 2-N, N-diethylamino-9,9-dibutyl-7-(4,6-bis(3,5-dimethylpyrazolyl)-1,3,5-triazin-2-yl)fluorine, which shows the unusual thermally promoted sensitization of Yb^{3+} luminescence, and its excellent performance can be used as a NIR-emission temperature-sensing material. To the best of our knowledge, the compounds with emission being sensitive to temperature have being seldom reported regarding the luminescence compounds, which luminescent nature is sensitive to oxygen, humidity in air, ions in solution, acids or bases, volatile organic compounds.

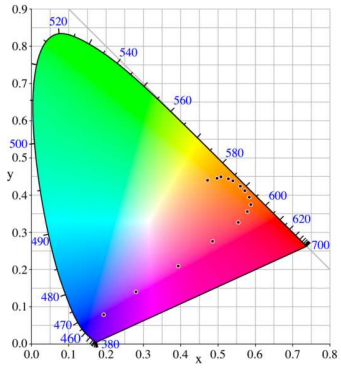

Fig. 9: CIE chromaticity diagram showing the fluorescence color of **1** at selected temperatures.

Conclusion

In summary, we designed and prepared a bi-functional hybrid solid [1, 5-bis(1-methylimidazolium)pentane][$PbBr_3$]$_2$ via introducing imidazolium derivatives with low rotation energy barrier into inorganic [$PbBr_3$]$_\infty$ lattice. The hybrid shows dielectric anomaly at ca. 443 K, and dielectric relaxation at the temperature above 400 K. The study of frequency-dependent dielectric spectra and impedance spectra

revealed that the dielectric relaxation is related to the orientation motion of imidazole rings in the cations and relative displacements of cations with regard to rigid $[PbBr_3]_\infty$ chain. The hybrid emits dual band fluorescence, which two emission bands exhibit distinct response to temperature, such novel nature has promising application in the emission temperature-sensing field. This study suggested that we probably achieve the multi-functional hybrid materials via integrating different functionality building blocks in a hybrid lattice.

Acknowledgements

Authors thank the Priority Academic Program Development of Jiangsu Higher Education Institutions, Special Research Found for the Doctoral Program of Higher Education and the National Nature Science Foundation of China (grant no. 20123221110013, 21201103 and 21271103) for financial support.

References

1. M. E. Itkis, X. Chi, A. W. Cordes, R. C. Haddon, Science 2002, 296, 1443
2. E. Coronado, J. R. Galán-Mascarós, C. J. Gómez-García, V. Laukhin, Nature 2000, 408, 447.
3. O. Kahn, C. J. Martinez, Science 1998, 279, 44.
4. M. W. Gaultois, P. T. Barton, C. S. Birkel, L. M. Misch, E. E. Rodriguez, G. D. Stucky, R. Seshadri, J. Phys.: Condens. Matter 2013, 25, 186004.
5. B. C. Melot, A. Goldman, L. E. Darago, J. D. Furman, E. E. Rodriguez, R. Seshadri, J. Phys.: Condens. Matter 2010, 22, 506003.
6. T. Dietl, Nat. Mater. 2010, 9, 965
7. J. K. Furdyna, J. Appl. Phys. 1988, 64, R29.
8. Y. D. Kim, S. L. Cooper, M. V. Klein, B. T. Jonker, Phys. Rev. B 1994, 49, 1732.
9. H. Ohno, D. Chiba, F. Matsukura, T. Omiya, E. Abe, T. Dietl, Y. Ohno, K. Ohtani, Nature 2000, 408, 944.
10. D. Chiba, M. Sawicki, Y. Nishitani, Y. Nakatani, F. Matsukura, H. Ohno, Nature 2008, 455, 515.
11. S. Cheong, M. Mostovoy, Nat. Mater. 2007, 6, 13.
12. W. Eerenstein, N. D. Mathur, J. F. Scott, Nature 2006, 442, 759.
13. H. Sun, S. Liu, W, Lin, K. Y. Zhang, W. Lv, X. Huang, F. Huo, H. Yang, G. Jenkins, Q. Zhao, W. Huang, *Nat. Commun.* 2014, **5**:3601.
14. P. Y. Gu, J. Gao, Q. Zhang, G. Liu, F. Zhou, Q. F. Xu, J. M. Lu, *J. Mater. Chem. C* 2014, **2**, 1539.
15. B. He, J. Dai, D. Zherebetskyy, T. L. Chen, B. A. Zhang, S. J. Teat, Q. Zhang, L. Wang, Y. Liu, *Chem. Sci.* 2015, **6**, 3180.
16. H. Y. Li, Y. L. Wei, X. Y. Dong, S. Q. Zang, T. C. W. Mak, *Chem. Mater.* 2015, **27**, 1327.
17. C. F. Wang. R. F. Li, X.Y. Chen, R. J. Wei, L. S. Zheng, J. Tao, *Angew. Chem. Int. Ed.* 2015, **54**, 1574.
18. D. G. Billing, A. Lemmerer, *CrystEngComm* 2006, **8**, 686.

19. A. Lemmerer, D. G. Billing, *CrystEngComm* 2012, **14**, 1954.
20. Y. Li, G. Zheng, C. Lin, J. Lin, *Cryst. Growth & Des.* 2008, **8**, 1990.
21. N. Louvain, N. Mercier, *Solid State Sci.* 2008, **10**, 1269.
22. T. Zhang, M. Yang, E. E. Benson, Z. Li, J. van de Lagemaat, J. M. Luther, Y. Yan, K. Zhu, Y. Zhao, *Chem. Commun.* 2015, **51**, 7820.
23. E. R. Dohner, E. T. Hoke, H. I. Karunadasa, *J. Am. Chem. Soc.* 2014, **136**, 1718.
24. E. R. Dohner, A. Jaffe, L. R. Bradshaw, H. I. Karunadasa, *J. Am. Chem. Soc.* 2014, **136**, 13154.
25. M. A. Garcia-Garibay, *Proc. Natl. Acad. Sci.* U. S. A., 2005, **102**, 10771.
26. S. Cortnie, M. A. Garcia-Garibay, *Chem. Soc. Rev*. 2012, **41**, 1892.
27. W. Liao, G. Mei, H. Ye, Y. Mei, Y. Zhang, *Inorg. Chem*. 2014, **53**, 8913.
28. W. H. Ning, L. Zhai, X. M. Ren, *RSC Adv.* 2014, **4**, 30993.
29. A. Piecha, A. Gągor, A. Pietraszko, R. Jakubas, *J. Solid State Chem.* 2010, **183**, 3058.
30. H. B. Cui, K. Takahashi, Y. Okano, H. Kobayashi, Z. M. Wang, A. Kobayashi, *Angew. Chem. Int. Ed.* 2005, **44**, 2.
31. R. Decressain, R. Jakubas, G. Bator, J. Zaleski, J. Lefebvre, J. Kusz, *J. Phys. Chem. Solids* 1999, **58**, 1487.
32. W. Zhang, H. Y. Ye, R. Graf, H. W. Spiess, Y. F. Yao, R. Q. Zhu and R. G. Xiong, *J. Am. Chem. Soc.*, 2013, **135**, 5230.
33. P. Zhou, Z. Sun, S. Zhang, C. Ji, S. Zhao,R. G. Xiong, J, Luo. *J. Mater. Chem. C*, 2014, **2**, 2341.
34. S. S. Yu, H. B. Duan, X. R. Chen, Z. F. Tian, X. M. Ren. *Dalton Trans.*, 2013, **42**, 3827.
35. *Software packages SMART and SAINT*, Siemens Analytical X-ray Instrument Inc., Madison, WI, 1996.
36. G. M. Sheldrick, *SHELX-97, Program for the refinement of crystal structure*, University of Göttingen, Germany, 1997.
37. A. Thirumurugan and C. N. R. Rao, *Cryst. Growth & Des.* 2008, **8**, 1640.
38. R. Perochon, P. Davidson, S. Rouzière, F. Camerel, L. Piekara-Sady, T.

Guizouarn, M. Fourmigué, *J. Mater. Chem.* 2011, **21**, 1416.

39. Y. Molard, F. Dorson, V. Cîrcu, T. Roisnel, F. Artzner, S. Cordier, *Angew. Chem. Int. Ed.* 2010, **49**, 3351.
40. S. Karoui, S. Kamoun, A. Jouini, *J. Solid State Chem.* 2013, **197**, 60.
41. Q. Chen, P. C. Guo, S. P. Zhao, J. L. Liu, X. M. Ren, *CrystEngComm* 2013, **15**, 1264.
42. Azuma, J.; Tanaka, K.; Kan'no, K.-i. *J. Phys. Soc. Jpn.* 2002, **71**, 971.
43. O. S. Wenger, *Chem. Rev.* 2013, **113**, 3686.
44. M. Tang, Y. Huang, Y. Wang, L. Fu, *Dalton Trans.* 2015, **44**, 7449.

Table 2: Atom displacement parameters (U_{eq}, U_{11}, U_{22} and U_{33}) of **1** at 298, 373 and 441 K

	U_{eq} / (10^{-2})Å^2			U_{11} / (10^{-2})Å^2			U_{22} / (10^{-2})Å^2			U_{33} / (10^{-2})Å^2		
T / K	298	373	441	298	373	441	298	373	441	298	373	441
Pb(1)	4.01(2)	5.59(4)	6.29(5)	3.94(3)	5.55(6)	6.33(7)	4.22(3)	5.83(7)	6.64(8)	3.88(3)	5.37(6)	5.91(7)
Br(1)	4.96(4)	6.81(9)	7.76(9)	4.07(8)	5.51(13)	6.40(14)	5.23(8)	7.14(18)	8.32(19)	5.57(8)	7.77(18)	8.58(19)
Br(2)	6.27(5)	8.36(10)	9.35(11)	4.81(9)	7.10(17)	7.94(17)	6.38(9)	8.1(2)	9.2(2)	7.6(1)	9.8(2)	10.9(2)
Br(3)	6.00(4)	8.27(9)	9.31(10)	6.5(1)	9.58(18)	11.01(19)	4.01(7)	5.33(17)	6.05(18)	7.52(9)	9.9(2)	10.9(2)
N(1)	6.5(4)	8.2(8)	9.2(9)	5.5(10)	5.7(14)	7.3(15)	3.2(7)	4.3(15)	3.9(14)	10.9(12)	15(3)	16(3)
N(2)	5.4(3)	6.6(6)	7.7(6)	5.0(8)	6.0(13)	6.7(13)	4.9(7)	5.3(15)	6.8(16)	6.2(7)	8.5(16)	9.5(17)
C(1)	18(2)	21(4)	27(7)	8(3)	18(7)	34(16)	19(5)	6(4)	7(4)	29(7)	39(14)	41(18)
C(2)	7.6(12)	37(7)	31(6)	7(2)	24(7)	21(7)	10(2)	35(9)	32(11)	5.7(19)	53(13)	39(12)
C(2)’	7.0(20)			10(5)			4(3)			6(4)		
C(3)	9.6(7)	11.6(13)	13.7(16)	6.4(13)	10(2)	11(3)	5.9(10)	8(2)	7(2)	15.9(2)	18(4)	23(5)
C(4)	4.9(3)	6.7(7)	7.8(7)	4.7(9)	7.6(17)	9.3(19)	3.3(8)	3.1(15)	5.3(18)	6(4)	10(2)	8.8(19)
C(5)	7.9(5)	10.2(11)	12.6(15)	7.6(13)	8(2)	8(2)	8.6(13)	12(3)	18(5)	8.6(13	10(2)	12(3)
C(6)	7.1(6)	8.8(11)	10.6(12)	5.2(12)	7(2)	11(3)	4.9(10)	8(3)	8(3)	4.9(10)	11(3)	13(3)
C(7)	7.2(5)	10.1(11)	12.2(13)	6.2(12)	13(3)	14(3)	5.9(10)	6(2)	6(2)	5.7(10)	11(3)	16(3)